Research in Astron. Astrophys. **XXXX** Vol. **X** No. **XX**, 000–000
http://www.raa-journal.org   *http://www.iop.org/journals/raa*

***R**esearch in*
***A**stronomy and*
***A**strophysics*

arXiv:1103.5540v1 [astro-ph.CO] 29 Mar 2011

^{12}CO, ^{13}CO and C^{18}O observations along the major axes of nearby bright infrared galaxies

Q.H. Tan[1,2,3], Yu Gao[1], Z.Y. Zhang[1,2] and X.Y. Xia[3]

[1] Purple Mountain Observatory, Chinese Academy of Sciences, Nanjing 210008, China
qhtan@pmo.ac.cn
[2] Graduate School of Chinese Academy of Sciences, Beijing 100039, China
[3] Center of Astrophysics, Tianjin Normal University, Tianjin 300384, China Received [0] [0] [0];

accepted [0] [0] [0]

Abstract We present simultaneous observations of ^{12}CO, ^{13}CO and C^{18}O J=1$-$0 emission in 11 nearby (cz <1000 km s^{-1}) bright infrared galaxies. Both ^{12}CO and ^{13}CO are detected in the centers of all galaxies, except for ^{13}CO in NGC 3031. We have also detected C^{18}O, CSJ=2$-$1, and HCO$^+$ J=1$-$0 emission in the nuclear regions of M82 and M51. These are the first systematical extragalactic detections of ^{12}CO and its isotopes from the PMO 14m telescope.
We have conducted half-beam spacing mapping of M82 over an area of $4' \times 2.5'$ and major axis mapping of NGC 3627, NGC 3628, NGC 4631, and M51. The radial distributions of ^{12}CO and ^{13}CO in NGC 3627, NGC 3628, and M51 can be well fitted by an exponential profile. The ^{12}CO/^{13}CO intensity ratio, $\mathcal{R}$, decreases monotonically with galactocentric radius in all mapped sources. The average $\mathcal{R}$ in the center and disk of the galaxies are 9.9±3.0 and 5.6±1.9 respectively, much lower than the peculiar $\mathcal{R}$(∼24) found in the center of M82.
The intensity ratios of ^{13}CO/C^{18}O, ^{13}CO/HCO$^+$ and ^{13}CO/CS (either ours or literature data) show little variations with galactocentric radius, in sharp contrast with the greatly varied $\mathcal{R}$. This supports the notion that the observed gradient in $\mathcal{R}$ could be the results of the variations of the physical conditions across the disks. The H$_2$ column density derived from C^{18}O shows that the Galactic standard conversion factor (X-factor) overestimates the amount of the molecular gas in M82 by a factor of ∼2.5. These observations suggest that the X-factor in active star-forming regions (i.e., nuclear regions) should be lower than that in normal star-forming disks, and the gradient in $\mathcal{R}$ can be used to trace the variations of the X-factor.

Key words: galaxies: ISM— ISM: clouds — ISM: molecules — radio lines: ISM

1 INTRODUCTION

It is well known that molecules constitute a significant fraction of the interstellar medium (ISM) and stars form from molecular clouds. However, the most abundant molecule, H$_2$, cannot be detected directly in typical cold (10-40 K) molecular cloud, owing to its lack of a permanent electric dipole moment. The next most abundant molecule is ^{12}CO, which is found to be an excellent tracer of H$_2$ due to the low excitation temperature (∼10 K) and critical density (∼300 cm^{-3}) (Evans 1999). Generally, the lowest transition (J=1$-$0) of the rotational lines of ^{12}CO and its optically thin isotopic variants (e.g., ^{13}CO and $C^{18}O$) can be used to estimate the column density ($N(H_2)$) of molecular clouds in our Galaxy (Frerking et al. 1982; Young & Scoville 1982; Wilson et al. 2009). However, up to now, the column density of molecular gas in galaxies is difficult to obtain directly in this way due to the beam dilution and the weakness of line emission in CO isotopes. Accurate determination of the H_2 column densities from CO observations has therefore been a longstanding challenge in external galaxies.

In our Galaxy, results from independent methods show a tight correlation between the integrated ^{12}CO line intensity $I_{^{12}\mathrm{CO}}$ and $N(H_2)$, and the ratios of $N(H_2)$ to $I_{^{12}\mathrm{CO}}$ appear to be constant with values of (1-5)$\times 10^{20}\,\mathrm{cm}^{-2}\mathrm{K}^{-1}\mathrm{km}^{-1}$s across the Galaxy (Bohlin et al. 1978; Dickman 1978; Hunter et al. 1997; Scoville et al. 1987; Young & Scoville 1991). This constant value is denoted as the ^{12}CO-to-H_2 conversion factor, or the X-factor ($X \equiv N(H_2)/I_{^{12}\mathrm{CO}}$). It is beyond the scope of this paper to analyze in great detail the origin of the empirical 'X-factor' since many studies have shown that the X-factor varies with different physical conditions and environments, and is influenced by the CO abundance, the gas excitation and the radiative transfer processes (Scoville & Solomon 1974). For example, the amounts of molecular gas in the metal-poor Magellanic Clouds and M31 were claimed to be underestimated by up to a factor of $\sim$10 if a standard Galactic X-factor was adopted (Maloney & Black 1988; Allen & Lequeux 1993; Israel 1997). Nevertheless, recent imaging of CO clouds reports similar standard X-factor in metal-poor galaxies (Bolatto et al. 2008). Conversely, the amounts of molecular gas in the ultraluminous infrared galaxies (ULIRGs) might be overestimated by factors of $\sim$5 (Downes & Solomon 1998) using the standard Galactic X-factor.

The $IRAS$ all-sky survey has revealed a large population of infrared bright galaxies with bulk energy emission in the far-infrared (Soifer et al. 1987; Sanders et al. 2003), which is mostly due to dust heating from starburst (Sanders & Mirabel 1996). Early numerous CO observations of infrared galaxies found that these galaxies are rich in molecular gas (Young et al. 1995), and there exist a correlation between CO and far-infrared luminosity (Solomon & Sage 1988; Young & Scoville 1991), though the correlation is non-linear (Gao & Solomon 2004b) since $L_{\mathrm{IR}}/L_{\mathrm{CO}}$ correlates with L_{IR}. Moreover, recent studies on high-redshift star forming galaxies further confirmed the validity of CO-IR luminosity correlation (Solomon & Vanden Bout 2005; Daddi et al. 2010).

Although large quantities of observational studies have aimed at mapping the molecular gas distribution/kinematics in nearby infrared bright galaxies with single-dish and/or interferometer telescopes (Braine et al. 1993; Young et al. 1995; Sakamoto et al. 1999; Nishiyama et al. 2001; Helfer et al. 2003; Leroy et al. 2009), these surveys are almost all based on the observations of CO J=1$-$0 or J=2$-$1, and only limited systematical studies of CO isotope variants such as ^{13}CO, have been published so far (Paglione et al. 2001). Owing to the large isotope abundance ratio [^{12}CO]/[^{13}CO]$\approx$30-70 across the Galaxy (Langer & Penzias 1990), the opacity of ^{13}CO is much lower than that of ^{12}CO, and thus ^{13}CO is believed to be mostly optical thin and trace the molecular gas column density adequately in most cases. Consequently, the variations in the intensity ratio of ^{12}CO to ^{13}CO as a function of galactocentric radius, could give a reliable test of whether X-factor varies systematically within galaxies. Studies of the Galactic X-factor have revealed large variations in its value towards the Galactic nuclear region, with an order of magnitude increase from the center to the outer disk (Sodroski et al. 1995; Dahmen et al. 1998). In other galaxies, however, Rickard & Blitz (1985) claimed that the value of integrated intensity ratio of ^{12}CO to ^{13}CO in the nucleus is on average a factor of two higher than that in the disk. In fact, both Young & Sanders (1986) and Sage & Isbell (1991) suggested that there was no clear evidence of a systematic difference in $\mathcal{R}$ within a galaxy, and they suggested that the variations in $\mathcal{R}$ observed by Rickard & Blitz (1985) is likely to be caused by pointing errors. Recently, mapping surveys of ^{12}CO and ^{13}CO emission towards a large sample of nearby galaxies were carried out by Paglione et al. (2001), finding that the same physical processes (e.g., the molecular gas kinetic temperature) may both affect $\mathcal{R}$ and X-factor, moreover, the latter is also expected to decrease from the disks to the nuclear regions by factors of 2-5.

However, any study of the physical properties of molecular gas that involves using line intensity ratios might be influenced by measurement errors, owing to the telescopes' different beam sizes, uncertain beam efficiencies, pointing errors, and calibrations. Recently updated and improved sensitivity and system performance with the Purple Mountain Observatory (PMO) 14m telescope at Delingha, China allow us to simultaneously observe extragalactic sources systematically in ^{12}CO, ^{13}CO, and C^{18}O for the first time. Consequently, our simultaneous observations of three CO isotope variants with same telescope are better suited to obtain the well-calibrated line intensity ratios than observations from different telescopes carried out with different tunings at different time.

In this paper, we present the results of simultaneous observations of ^{12}CO, ^{13}CO, and C^{18}O along the major axes in nearby infrared bright galaxies. The sample selection, observations, and data reduction are described in § 2; the observed CO spectra, CO radial distributions, and position-velocity diagrams are presented in § 3. These results together with the radial distributions of molecular gas, CO isotopic ratio $\mathcal{R}$, and possible physical mechanisms that could be responsible to the observed variations in $\mathcal{R}$ are discussed in § 4. Finally a summary is presented in § 5. A stability analysis of the PMO 14m telescope is presented in Appendix A.

2 SAMPLE, OBSERVATIONS AND DATA REDUCTION

The galaxies in this study were selected from the Revised Bright Galaxy Sample (RBGS, Sanders et al. , 2003). We selected 11 galaxies based on the following three criteria: (1) $f_{60\mu m} \geq 50$ Jy or $f_{100\mu m} \geq$ 100 Jy. This infrared flux cutoff was chosen to ensure both ^{12}CO and ^{13}CO could be detected with reasonable integration time since it is well known that the infrared luminosity of galaxies is correlated with the CO luminosity (e.g., Solomon & Sage , 1988). (2) $cz \leq 1000\,\mathrm{km\ s^{-1}}$. This velocity limit was chosen due to the limited tuning range of the SIS receiver with the PMO 14m telescope. (3)9h$\leq$ R.A. $\leq$15h and Decl.$\geq 0^\circ$. For the reason that we can take full advantage of the Galactic dead time to observe galaxies in the northern sky. Some general properties of the sample galaxies are summarized in Table 1.

Our observations were made between 2008 January and 2009 December using the PMO 14m millimeter telescope at the Delingha. We used the 3mm SIS receiver operated in double-sideband mode, which allowed for simultaneous observations of three CO isotope variants, with ^{12}CO in the upper sideband and ^{13}CO and C^{18}O in the lower sideband. The Half Power Beam Width (HPBW) is $\sim 60''$, and the main beam efficiency $\eta_{\rm mb}$ = 0.67. Typical system temperatures during our runs were about 180-250 K. The FFT spectrometer was used as back end with a usable bandwidth of 1 GHz and a velocity resolution of 0.16 $\mathrm{km\ s^{-1}}$ at 115GHz. Observations were done in position switching mode and calibrated using the standard chopper wheel method. The absolute pointing uncertainty was estimated to be $\sim$10$''$ from continuum observations of planets, and the pointing were checked every two hours by taking spectra toward the standard source IRC+10216 throughout our observations. Each galaxy was first observed at the center position, and then along its major axis from the center to the outer disk positions separated by half-beam size. Besides the CO observations, we also observed the dense molecular gas tracers HCO$^+$ and CS in the nuclear regions of galaxies.

The data were reduced using CLASS, which is part of the GILDAS[1] software package. All scans were individually inspected, and those with either strongly distorted baselines or abnormal rms noise levels were discarded. Line-free channels which exhibited positive or negative spikes more than 3 σ above the rms noise were blanked and substituted with values interpolated from the adjacent channels, and then a linear baseline was subtracted from the 'line-free' spectrum. After correcting each spectrum for main beam efficiency $\eta_{\rm mb}$, the temperature scale of the spectra was converted to the main beam temperature $T_{\rm mb}$ scale from the T_A^*. The spectra were then co-added, weighted by the inverse of their rms noises, and the final spectral resolution was smoothed to $\sim$20 $\mathrm{km\ s^{-1}}$.

Since this is the first time that the PMO 14m millimeter telescope systematically observed galaxies other than our own, relatively rather long observing time at each pointing is devoted to accumulate relatively adequate integration time. Thus our observations are the first long integrations for the PMO 14m telescope ever conducted and offer an excellent opportunity to test the stability of the upgraded system (see Appendix A). The work present here represents the total of $\sim$ 500 hours observing time in CO observations before the telescope system maintenance in the summer of 2009 at the PMO 14m and

---

[1] http://iram.fr/IRAMFR/GILDAS/

$\sim$ 200 hours after the upgrade, with $\sim 40\%$ data discarded owing to the unstable spectrum baseline and bad weather conditions.

3 RESULTS AND ANALYSIS

3.1 CO Isotopic Spectra

We detected ^{12}CO emission from the centers of all 11 galaxies observed, of which 10 were also detected in ^{13}CO simultaneously. Four galaxies (NGC 3627, NGC 3628, NGC 4631 and M51) were observed along the major axes, and ^{12}CO emission was detected at all 42 off-center positions along the major axes, while ^{13}CO was detected at 27 out of the 42 positions. For M82, the starburst galaxy, ^{12}CO emission was detected at all 47 positions that were mapped in the central $4' \times 2.5'$ region, while ^{13}CO was tentatively detected at 15 positions. C^{18}O emission was only detected at 13 points close to the nuclear regions in M51 and M82.

Here, we focus on presenting ^{13}CO and C^{18}O spectra as compared to ^{12}CO observed simultaneously at the same positions, ^{12}CO spectra at those ^{13}CO undetected positions won't be shown here. Since many previous observations of ^{12}CO emission in these galaxies are available in literature (e.g., Young et al. , 1995), and our ^{12}CO observations show similar results and comparable spectra. The spectra of both ^{12}CO and ^{13}CO, as well as *Spitzer* IRAC 3.6 μm, 8 μm and MIPS 24 μm infrared composite color images showing the observed beam positions of the mapped galaxies, are shown in Fig.1. All the three CO isotopic spectra at these C^{18}O detected positions are shown in Fig. 2.

3.2 Derived Parameters

The observational results and derived properties are summarized in Table 2. The velocity-integrated ^{12}CO (and isotopes) intensity, $I_{\rm CO} \equiv \int T_{\rm mb} dv$, is obtained by integrating $T_{\rm mb}$ over the velocity range with CO line emission feature. Using the standard error formulae in Gao (1996) (also in Matthews & Gao , 2001), the error in the integrated intensity is

$$\Delta I = T_{\rm rms}\, \Delta v_{\rm FWZI} / [f\ (1 - \Delta v_{\rm FWZI}/W)]^{1/2}\ [{\rm K\ km\ s^{-1}}], \tag{1}$$

where $T_{\rm rms}$ is the rms noise in the final spectrum in mK, $f = \Delta v_{\rm FWZI}/\delta_v$, where $\Delta v_{\rm FWZI}$ is the linewidth of the emission feature, δ_v is the channel bin spacing, and W is the entire velocity coverage of the spectrum in units of kilometers per second. For non-detections (only CO isotopes), some spectra are further smoothed and found to be marginally detected with signal-to-noise of $\sim$2.5. Otherwise, a 2 σ_I upper limits are given based on the estimation by using the expected line width from the detected ^{12}CO lines at exactly the same position.

The H$_2$ column density and mass surface density for galaxies in our sample are derived from the empirical relations (Nishiyama et al. 2001)

$$N({\rm H_2})[{\rm cm^{-2}}] = 2 \times 10^{20} I_{^{12}{\rm CO}} [{\rm K\ km\ s^{-1}}], \tag{2}$$

and

$$\Sigma({\rm H_2})[M_\odot {\rm pc^{-2}}] = 3.2 I_{^{12}{\rm CO}} [{\rm K\ km\ s^{-1}}] {\rm cos}i, \tag{3}$$

where cos$i$ corrects the mass to face-on and a Galactic ^{12}CO-to-H$_2$ conversion factor X=2.0$\times$10^{20} cm^{-2}K^{-1}km^{-1}s is adopted (Dame et al. 2001). Obviously, it can be seen from Table 2 that the column density in M82 is usually a magnitude higher than that in normal spiral galaxies (the rest of the sample).

Assuming that ^{13}CO has the same excitation temperature as ^{12}CO and the molecular cloud is under LTE conditions, then we can calculate the average ^{13}CO optical depth from

$$\tau(^{13}{\rm CO}) = \ln[1 - \frac{\int T_R^*(^{13}{\rm CO}) dv}{\int T_R^*(^{12}{\rm CO}) dv}]^{-1}, \tag{4}$$

where T_R^* should be corrected for filling factor, and we can only estimate an average over all of the unresolved clouds in the beam. Using the definition in Wilson et al. (2009), the H$_2$ column density can be derived from the ^{13}CO line intensity as

$$N(\mathrm{H_2})(^{13}\mathrm{CO}) = [\frac{\tau(^{13}\mathrm{CO})}{1-e^{-\tau(^{13}\mathrm{CO})}}]2.25\times10^{20}\frac{\int T_{\mathrm{mb}}(^{13}\mathrm{CO})dv}{1-e^{-5.29/T_{\mathrm{ex}}}}, \tag{5}$$

where the ^{13}CO abundance [^{13}CO]/[H$_2$] is 8×10^{-5}/60 (Frerking et al. 1982) and the excitation temperature, T_{ex}, is taken to be the kinetic temperature of the gas, T_{K}. Thus, we can estimate T_{K} by equating the column densities derived from both ^{12}CO and ^{13}CO. Both the derived $\tau(^{13}\mathrm{CO})$ and T_{K} are listed in Table 2. Note that LTE assumption is most likely invalid in the central regions of M82. Therefore, the extremely low optical depth of ^{13}CO ($\sim$0.04) should be treated only as a lower limit, and the resulting kinetic temperature (between 70 and 120 K), which are about 3-4 times higher than that in normal galaxies, should be treated as an upper limit.

Similarly, we estimated the optical depth of C^{18}O adopting the same method as equation (4), and derived the H$_2$ column density from C^{18}O intensity using (Sato et al. 1994)

$$N(\mathrm{H_2})(\mathrm{C^{18}O}) = [\frac{\tau(^{18}\mathrm{CO})}{1-e^{-\tau(^{18}\mathrm{CO})}}]1.57\times10^{21}\frac{\int T_{\mathrm{mb}}(\mathrm{C^{18}O})dv}{1-e^{-5.27/T_{\mathrm{ex}}}}, \tag{6}$$

where the abundance of [C^{18}O]/[H$_2$] is 1.7×10^{-7} (Frerking et al. 1982) and T_{ex} is adopted from the value listed in Table 2. The derived values of $\tau(\mathrm{C^{18}O})$ and $N(\mathrm{H_2})(\mathrm{C^{18}O})$ for the 13 points of M82 and M51 detected in C^{18}O are listed in Table 3. The average optical depths of C^{18}O in M82 and M51 are 0.02 and 0.05 respectively, both are about three times lower than that of ^{13}CO. Therefore, although the optical depth of ^{13}CO is moderate ($\tau(^{13}\mathrm{CO})$ $\sim$0.3–0.4) in a few galaxies (e.g., NGC 3627 and NGC 4631; see Table 2), C^{18}O is always optically thin in all cases here.

3.3 Distribution of CO Isotopes and Line Ratios

The distributions of ^{12}CO and ^{13}CO velocity-integrated intensities and their ratio $\mathcal{R}$ as a function of galacto-central radius are shown in Fig. 3. Note that none of these profiles have been corrected for inclination. Both the ^{12}CO and ^{13}CO emission line intensities show an exponential decrease with radius, and the ratio $\mathcal{R}$ decreases from nucleus to the outer disk.

3.3.1 Radial distributions of ^{12}CO and ^{13}CO

The obvious trends shown in Fig. 3 are that the observed radial distribution of ^{13}CO follows that of ^{12}CO. The integrated line intensities usually peak in the center of galaxies and fall monotonically toward larger galactocentric radii. For the barred spiral galaxies NGC 3627 and NGC 4631, however, both ^{12}CO and ^{13}CO intensities peak at radius of $\sim$ 1 kpc ($\sim$0.5') rather than at the nuclei. The same feature has also been presented in Paglione et al. (2001) for NGC 4631. Some previous high resolution observations of barred galaxies revealed that the molecular gas was concentrated in the central regions, with secondary peaks at the bar ends due to the bar potential and the viscosity of the gas (Regan et al. 1999; Sakamoto et al. 1999).

Similar to the stellar luminosity profiles, the observed ^{12}CO radial distributions in NGC 3627, NGC 3628 and M51 could also be well fitted by an exponential fit in R

$$I(R) = I_0\exp{(-R/R_0)}, \tag{7}$$

where R is the galactocentric distance, R_0 is the disk scale length, and I_0 is the central integrated intensity. The solid curves in Fig. 3 show the least-squares fit to the data excluding the center point as the nuclear gas could be a distinct component, yielding I_0 = 32.6 K km s^{-1} and R_0 = 3.5 kpc for the ^{12}CO emission in NGC 3628, I_0 = 37.8 K km s^{-1} and R_0 = 2.7 kpc and I_0 = 3.5 K km s^{-1} and R_0 = 3.8 kpc for ^{12}CO and ^{13}CO emission in M51. In NGC 3627, the scale lengths are 2.8 kpc and

3.9 kpc for the ^{12}CO and ^{13}CO emission, respectively. However, the power law fit with functional form, $I = I_0\ R^{\alpha}$, is more suitable than exponential fit for the ^{12}CO distribution in NGC 4631. The fit result gives $\alpha = -1.5$ and I_0 = 41.1 K km s^{-1}. For the other three exponential fit galaxies, the power law could also fit ^{12}CO distribution almost equally well. The exponential ^{12}CO scale lengths of 2-4 kpc equal to $\sim$ 0.2 R_{25}, which is consistent with the results in Nishiyama et al. (2001). The distributions of ^{12}CO and ^{13}CO emission along the axis with position angle of 90° in M82 are similar to the other four galaxies. The distributions along the major axis are not shown here, since the observations of M82 were carried out by mapping an area of $4' \times 2.5'$.

3.3.2 The integrated line intensity ratios

The intensity ratio $\mathcal{R}$ ranges from 3.3±0.7 to 12.8±4.3 for all 36 points both detected in ^{12}CO and ^{13}CO emission from normal spiral galaxies, with mean value of 9.9±3.0 and 5.6±1.9 for the central and disk regions, respectively. However, the average $\mathcal{R}$ in M82 is about 2.5 times higher than that in the nucleus of normal spiral galaxies. We use the Equation (2) in Young & Sanders (1986) to calculate the mean value of $\mathcal{R}$ at each radius. The most prevalent trend is that the $\mathcal{R}$ drops at larger radius in both the barred and non-barred spiral galaxies that we have mapped along the major axis in our sample (Fig. 3). Here we note that two points ($\sim 2.5'$ away from center) are found to have significantly higher ratios (∼9) in M51. These abnormal high values in the disks are tended to be observed once the telescope beams are located in the most active star-forming regions along spiral arms.

The detection of C^{18}O in M82 and M51 also allow us to estimate the intensity ratio of ^{13}CO to C^{18}O, which ranges between 0.9±0.7 and 5.3±2.8 with mean value of 2.9±1.4. The ratios measured in the nucleus and disk of M51 are 3.7 and 2.6 respectively, agree well with the results of Vila-Vilaró (2008), which claimed first detect C^{18}O emission in the center of M51 with ^{13}CO/C^{18}O ratio of 3.6. Also the similar ^{13}CO/C^{18}O ratio values have been found in some starburst galaxies (e.g., Sage et al. , 1991; Aalto et al. , 1995). In addition, our detection of C^{18}O emission in the off-center regions of M51 represents the first report of such detection for this object by far.

Ongoing observations of dense gas tracers HCO^{+} and CS, toward the nuclear regions of NGC 4736, M82, NGC 3628, and M51 by far only yield detection in the latter three galaxies. Here, we also use these limited dense gas observations, along with the literature data, to help further analyze the CO isotopic results. The intensity ratios of ^{13}CO to HCO^{+} and ^{13}CO to CS are found to show little variations between starburst and normal galaxies, with average values of 1.3±0.3 and 3.2±1.4, respectively. The observed integrated intensity and line ratios and the literature data used are listed in Table 3.

3.4 Kinematics of CO

Figure 4 shows the CO position-velocity ($P - V$) diagrams along the major axes of the galaxies NGC 3627, NGC 3628, NGC 4631, and M51, and the $P - V$ diagrams with position angle of 0° and 90° in M82 as well. It can be seen in Fig. 4 that $P - V$ diagrams along the major axes tend to show a gradual increase of rotation velocity in the inner regions (rigid rotation) and a nearly constant velocity in the outer regions (differential rotation).

For NGC 3627 and M51, the $P - V$ spatial velocity maps of ^{13}CO are also shown in Fig. 4. Obviously, both ^{12}CO and ^{13}CO share essentially similar kinematics and distribution. At each position where observations were made, the distribution of line intensity and the velocity range for ^{12}CO and ^{13}CO emission are in good agreement. Accordingly, it could also hint that the line ratios at each position derived from our observations are relatively quite reliable.

Figure 5 shows the CO rotation curve and the variation in line width along the major axis. Using the mean velocities, inclination, systemic velocity, and position angle of the major axis that listed in Table 1, and by the assumption that the observed velocity reflect only the systemic motion of the whole galaxy and circular rotation, the rotation velocity $V_{\rm R}$ could be derived via

$$V_{\rm R} = (V_{\rm obs} - V_{\rm sys})/\sin i\ \cos\theta\,, \tag{8}$$

where $V_{\rm obs}$ is an observed velocity of ^{12}CO, $V_{\rm sys}$ is the systemic velocity of the galaxy, i is the inclination angle, and θ is the azimuth measured in the disk plane. The peak velocity, $V_{\rm max}$, in the rotation curve of our sample galaxies, ranges from 120 to 240 km s^{-1} ($V{\rm max}$ in spiral galaxies are usually between 150 and 300 km s^{-1}, Sparke & Gallagher , 2000).

4 DISCUSSION

4.1 Radial Distribution of Molecular Gas

In section 3.3, we show that the surface density of the molecular gas in the galaxies observed in our sample can be well fitted both by exponential and power law function. The χ^2 values indicate that the data fitting are at about 85% and 90% confidence level by the exponential and power law function, respectively. We are therefore unable to distinguish clearly between an exponential and a power law radial distribution over the regions observed here with limited sampling and low resolution. The similar conclusion has been pointed out in both Young & Scoville (1982) and Nishiyama et al. (2001). However, Scoville et al. (1983) considered that the exponential distribution was more suitable than that of power law for M51. The region in M51 observed by Scoville et al. (1983) is more extended ($\sim 8.5'$) than the region ($\sim 7'$) observed here, and thus the exponential functional form seems to be better for describing the distribution of molecular gas in the whole galaxy. In NGC 3627 and M51, the scale lengths R_0 of the ^{12}CO profiles agree well with the optical K-band scale lengths of 3.5 and 3.2 kpc (Regan et al. 2001), respectively. The results are in line with the finding first noted by Young & Scoville (1982) that the large-scale radial distribution of the ^{12}CO gas follows the light of the stellar disk. In fact, some recent high resolution observations also reveal that the ^{12}CO profiles in a majority of galaxies follow the two-component (bulge and disk) stellar brightness distribution quite well (Regan et al. 2001). The ^{13}CO profiles detected in our observations are in good agreement with that in Paglione et al. (2001). In NGC 3627 and M51, ^{13}CO profiles follow similar exponential distributions as ^{12}CO. Because of insufficient data points with significantly high signal-to-noise, however, the detected ^{13}CO data in other galaxies are too limited to reliably present more useful information on their distributions.

Comparing the radial distribution of CO integrated intensities in Fig. 3 with the $P-V$ map of CO emission intensities in Fig. 4, it is found that the intensities are deficient in the center of NGC 3627, NGC 4631, and M51. However, the centrally deficient feature in molecular ring emission is apparent in NGC 3627 and NGC 4631, but not in M51. So combining the variations in line width shown in Fig. 5, we believe the decrement of CO intensity in the central region of M51 is likely as a result of the dilution in velocity with much wider line width in the center than that in the outer regions of the central disk. On the contrary, the molecular ring emission features with little variations in line width within the bar region in NGC 3627 and NGC 4631, are probably either due to orbital disruption at the inner Lindblad resonance or the central holes with gas exhausted by star formation in the nuclei. Sakamoto et al. (1999) have modeled the $P-V$ diagrams to analyze gas distributions, and found that the central gas hole is easier to find from $P-V$ diagrams than from integrated intensity maps due to the velocity information.

4.2 Variations in the Intensity Ratio of ^{12}CO to ^{13}CO

Previous studies on the variations in $\mathcal{R}$ in external galaxies have pointed out that some mergers, LIRGs/ULIRGs, and the central regions of circumnuclear starburst galaxies tend to have higher values of $\mathcal{R}$ than that in normal spiral galaxies (Aalto et al. 1991, 1995; Casoli et al. 1992; Greve et al. 2009; Sage & Isbell 1991), of which is similar to that in giant molecular clouds of our Galaxy. Besides the enhancement of ^{12}C caused by nucleosynthesis from type-II SN of massive stars, the deficiency of ^{13}CO caused by isotope-selective photodissociation, and the different distributions of ^{12}CO and ^{13}CO were disputed to be alternative reasons for the high $\mathcal{R}$ value for a long time (Aalto et al. 1995; Casoli et al. 1992; Sage et al. 1991; Taniguchi et al. 1999). However, the single-component model calculation of non-LTE CO excitation in Paglione et al. (2001) suggested that the variations of kinetic temperature, cloud column and volume density, as well as starburst superwinds might all contribute to the explanations for the variation in $\mathcal{R}$. We here explore the possible causes of the observed variations in $\mathcal{R}$.

4.2.1 Possible causes of variations in $\mathcal{R}$

Our results show that $\mathcal{R}$ varies not only in the nuclei of various types of galaxies, but also within galaxies between nuclear regions and outer disks. The Galactic ^{12}C/^{13}C abundance ratio was found to range from $\sim$30 at 5 kpc in the Galactic center to $\sim$70 at 12 kpc (Langer & Penzias 1990). However, this isotopic gradient is opposite to the gradient in the molecular abundance ratio $\mathcal{R}$ (Fig. 3). Therefore, the enhancement of ^{12}C in starburst regions is unlikely to be an appropriate explanation for the measured high $\mathcal{R}$.

Some authors argue that the selective dissociation of ^{13}CO caused by ultraviolet (UV) field in massive star formation regions can stimulate the ratio of $\mathcal{R}$, since the rarer isotope is less shielded from photodissociation (van Dishoeck & Black 1988). Consequently, C^{18}O should be even more dissociated by UV photons than ^{13}CO due to its lower abundance, and a positive correlation between $\mathcal{R}$ and ^{13}CO/C^{18}O intensity ratio would expect to exist if this is available. However, Fig.6b shows a very marginal anti-correlation between $\mathcal{R}$ and ^{13}CO/C^{18}O with a correlation coefficient R=-0.34. Therefore, contrary to the expection, our results reveal a weak anti-correlation, and the deficiency of ^{13}CO caused by isotope-selective photodissociation could be ruled out.

In addition to the high $\mathcal{R}$ measured in M82, the integrated J=2-1/J=1-0 line ratio was found to range between 1.0 and 1.4 (Mao et al. 2000), revealing the existence of highly excited molecular gas. In the PDR model of Mao et al. (2000), it was suggested that the bulk of ^{12}CO emission arises from warm diffuse interclumpy medium whereas ^{13}CO emission originate in denser cores. In the warm PDRs, the optical depth of ^{12}CO emission from the envelope gas could decrease to a moderate value of $\tau \sim$1, result in the corresponding $\tau(^{13}\mathrm{CO}) << 1$. Moreover, the large concentrations of molecular gas in the nuclear starburst with high T_{K} can be excited by strong UV emission from young massive stars, shocks and turbulence caused by supernova remnants, and cosmic rays (Pineda et al. 2008; Zhang et al. 2010). The most recent $Herschel$ observations of M82 also suggested that turbulence from stellar winds and supernova may dominate the heating of warm molecular gas in the central region (Panuzzo et al. 2010). Therefore, it is likely to imply that nonthermal motions produced by the stellar superwinds can broaden ^{12}CO lines, thus enhance ^{12}CO emission as more photons located deeper in the clouds are allowed to escape. Furthermore, the significant high value of $\mathcal{R}$ observed in the spiral arms of M51 also demonstrate that ^{12}CO emission can be enhanced in active star-forming regions compared with that in inter-arm regions.

4.2.2 X-factor and dense gas ratio in extreme starburst

Both theoretical and observational investigations have revealed that ^{12}CO emission is influenced by the intrinsic properties of molecular cloud (e.g., Pineda et al. , 2008; Goodman et al. , 2009; Shetty et al. , 2011). In the magneto-hydrodynamic models of Shetty et al. (2011), ^{12}CO integrated intensity is found to be not an accurate measure of the amount of molecular gas, even for ^{13}CO, which may also not be an ideal tracer in some regions. In this case, the much lower opacity C^{18}O can give much more reliable constraints on H_2 column density than optically thick ^{12}CO isotopes. Comparing the H_2 column density derived from ^{12}CO with that from C^{18}O listed in Table 2 and Table 3, we find that the amount of molecular gas estimated by standard Galactic X-factor is consistent with that derived from C^{18}O in M51, whereas is overestimated in M82 by a factor of 2.5, equal to the ratio of $\mathcal{R}$ between M82 and M51. Consequently, our results confirm that the X-factor adopted in starburst active regions should be lower than that in normal star-forming regions, and the gradient in $\mathcal{R}$ can trace the variations in X-factor. However, surveys of C^{18}O in a larger sample are required to confirm the relation between the variations in $\mathcal{R}$ and X-factor found in this study.

The average ratio of ^{13}CO to C^{18}O ($\sim$2.9$\pm$1.4) derived from our observations in M51 and M82 indicates that a portion of ^{13}CO emission has a moderate optical depth, since the ratio of ^{13}CO to

C^{18}O should be $\sim$7 if both ^{13}CO and C^{18}O lines are optically thin (Penzias et al. 1981). This result is in line with the two-type cloud model suggested in Aalto et al. (1995), in which a large fraction of ^{13}CO emission might originate from denser gas component. Some previous surveys in dense molecule have provided support for the presence of such dense gas (e.g., Sage et al. , 1990; Nguyen et al. , 1992; Gao & Solomon , 2004a). In addition, our detection of HCO$^+$ and CS in M82 and M51 is consistent with that in Sage et al. (1990) and Naylor et al. (2010). The ratios of ^{13}CO to HCO$^+$ and ^{13}CO to CS in (U)LIRGs NGC 3256, NGC 6240 and Arp 220 (Casoli et al. 1992; Greve et al. 2009) are found to be lower than those in the nuclear regions of normal spirals and M82 (Fig. 6), which probably indicate that the dense gas fraction is higher for these (U)LIRGs, since ^{13}CO can be considered as a relative reliable tracer of total molecular gas due to its low abundance. This result agrees well with the conclusion in Gao & Solomon (2004b) that galaxies with high star formation efficiency tend to have higher dense gas fraction. Moreover, the ratio $\mathcal{R}$ measured in NGC 3256, NGC 6240 and Arp 220 are found to be much higher than those in M82 (Fig. 6), which is likely to imply that the bulk of ^{12}CO emission arise from warm diffuse gas is enhanced in the extreme starburst.

Summarizing the above analysis, the systematical gradient in $\mathcal{R}$ can be explained by the variations in the physical conditions of molecular gas. The standard Galactic X-factor used in M82 overestimates the amount of molecular gas by a factor of 2.5, and the variations in X-factor can be well traced by the gradient in $\mathcal{R}$. Nevertheless, additional observations of both ^{12}CO and ^{13}CO lines at J ≥ 2 and more C^{18}O lines are required to better constrain the physical conditions of the molecular gas in external galaxies.

5 SUMMARY

We observed simultaneously the ^{12}CO, ^{13}CO and C^{18}O emission lines in 11 nearby infrared-brightest galaxies, of which four (NGC 3627, NGC 3628, NGC 4631 and M51) were mapped with half-beam spacing along the major axes and M82 was fully mapped in an area of $4' \times 2.5'$. These are the first systematic extragalactic observations for the PMO 14m telescope and the main results are summarized as follows:

1.We detected the ^{12}CO emission towards 99 of the positions observed, with the ^{13}CO seen towards 51 of these. C^{18}O was detected at 13 positions close to the nuclear regions in M51 and M82, among which the off-center positions in M51 were the first C^{18}O detection reported here.

2.In the four galaxies with major axes mapping, the ^{13}CO line intensity decrease from center to outer disk, similar to that of ^{12}CO. In NGC 3627, NGC 3628, and M51, the radial distribution of both ^{12}CO and ^{13}CO can be well fitted by an exponential function, whereas the ^{12}CO distribution in NGC 4631 is better fitted by power law. The scale length of ^{12}CO emission is about 0.2 R_{25} with a mean value of $\sim$3 kpc. Moreover, the ^{12}CO scale lengths in NGC 3627 and M51 are in good agreement with the optical scale lengths.

3.The peak velocity of ^{12}CO rotation curves ranges from 120 to 240 km s^{-1}, and the line widths of ^{12}CO lines tend to drop with radius from center to outer disk in all mapped galaxies. Of all positions observed, the distribution of both line intensity and profiles of ^{12}CO and ^{13}CO have good agreement, as expected with simultaneously ^{12}CO and ^{13}CO observations. Thus, a reliable line intensity ratio $\mathcal{R}$ can be obtained.

4.A decreasing tendency of $\mathcal{R}$ with radius from center to outer disk is found in mapped galaxies. $\mathcal{R}$ varies from 3.3±0.7 to 24.8±2.5 in positions with both ^{12}CO and ^{13}CO detected. The average $\mathcal{R}$ are 9.9±3.0 and 5.6±1.9 in the center and disk regions of normal spiral galaxies,respectively.

5.The high $\mathcal{R}$ measured in M82 is likely to be caused by enhanced ^{12}CO emission from deeper cloud with broad ^{12}CO line produced by the stellar winds and supernova. The low values of ^{13}CO/C^{18}O ($\sim$2.8±1.2) found in M82 support the suggestion that a considerable fraction of ^{13}CO emission originates in denser gas component. Comparing the ratios of ^{13}CO/HCO$^+$ and ^{13}CO/CS in normal galaxies with those in U/LIRGs, the lower values found in U/LIRGs agree with the notion that the galaxies with high SFEs tend to have higher dense gas fraction.

6.Comparing with the H_2 column density derived from $C^{18}O$, the standard Galactic X-factor is found to overestimate the amount of molecular gas in M82 by a factor of $\sim$2.5. This confirms the assertion that a lower X-factor should be adopted in active starburst regions than that in normal star-forming disks, and moreover, the gradient in $\mathcal{R}$ can be used reliably to trace the variations of the X-factor.

Acknowledgements We thank the staff of Qinghai station for their continuous help. We are grateful to Thomas Greve and anonymous referee for helpful comments. This work was funded by NSF of China (Distinguished Young Scholars #10425313, grants #10833006 and #10621303) and Chinese Academy of Sciences' Hundred Talent Program.

References

Aalto, S., Black, J. H., Johansson, L. E. B., & Booth, R. S. 1991, A&A, 249, 323
Aalto, S., Booth, R. S., Black, J. H., & Johansson, L. E. B. 1995, A&A, 300, 369
Allen, R. J., & Lequeux, J. 1993, ApJ, 410, L15
Bohlin, R. C., Savage, B. D., & Drake, J. F. 1978, ApJ, 224, 132
Bolatto, A. D., Leroy, A. K., Rosolowsky, E., et al. 2008, ApJ, 686, 948
Braine, J., Combes, F., Casoli, F., et al. 1993, A&AS, 97, 887
Casoli,F., Dupraz, C., Combes, F. 1992, A&A, 264, 49
Daddi, E., Elbaz,D., Walter, F., et al. 2010, ApJ, 714, 118
Dame, T. M., Hartmann, D., & Thaddeus, P. 2001, ApJ, 547, 792
Dahmen,G., Huttemeister, S., Wilson, T. L., & Mauersberger, R. 1998, A&A, 331, 959
Dickman, R. L. 1978, ApJS, 37, 407
Downes, D., & Solomon, P. M. 1998, ApJ, 507, 615
Evans, N. J., II 1999, ARA&A, 37, 311
Frerking, M. A., Langer, W. D.,& Wilson, R. W. 1982, ApJ, 262, 590
Gao, Y. 1996, PhD. thesis, State Univ. New York, Stony Brook
Gao, Y., & Solomon, P. M. 2004a, ApJS, 152, 63
Gao, Y., & Solomon, P. M. 2004b, ApJ, 606, 271
Goodman, A. A, Pineda, J. E., & Schnee, S. L. 2009, ApJ, 692, 91
Greve, T. R., Papadopoulos, P. P. P., Gao, Y., & Radford, S. J. E. 2009, ApJ, 692, 1432
Helfer, T. T, Thornley, M. D., Regan, M. W., et al. 2003, ApJS, 145, 259
Henkel, C., Mauersberger, R., Wiklind, T., et al. 1993, A&A, 268, L17
Hunter, S. D., Bertsch, D. L., Catelli, J. R., et al. 1997, ApJ, 481, 205
Israel, F. P. 1997, A&A, 328, 471
Langer, W. D., & Penzias, A.A. 1990, ApJ, 357, 477
Leroy, A. K., Walter, F., Bigiel, F., et al. 2009, AJ, 137, 4670
Maloney, P., & Black, J. H. 1988, ApJ, 325, 389
Mao, R. Q., Henkel, C., Schulz, A., et al. 2000, A&A, 358, 433
Matthew, L. D., & Gao, Y. 2001, ApJ, 549, L191
Naylor, B. J., Bradford, C. M., Aguirre, J. E., et al. 2010, ApJ, 722, 668
Nishiyama, K., Nakai, N., & Kuno, N. 2001, PASJ, 53, 757
Nguyen, Q. -Rieu, Jackson, J. M., Henkel, C., et al. 1992, ApJ, 399, 521
Paglione, T. A. D., Wall, W. F., Young, J. S., et al. 2001, ApJS, 135, 183
Panuzzo, P., Rangwala, N., Rykala, A., et al. 2010, A&A, 518, L37
Penzias, A. A. 1981, ApJ, 249, 518
Pineda, J. E., Caselli, P., & Goodman, A. A. 2008, ApJ, 679, 481
Regan, M. W., Sheth, K., &Vogel, S. N. 1999, ApJ, 526, 97
Regan, M. W., Thornley, M. D., Tamara, T. H., et al. 2001, ApJ, 561, 218
Rickard, L. J., & Blitz, L. 1985, ApJ, 292, L57
Sage, L. J., Shore, S. N., & Solomon, P. M. 1990, ApJ, 351, 422

Sage, L. J., & Isbell, D. W. 1991, A&A, 247, 320
Sage, L. J., Mauersberger, R., & Henkel, C. 1991, A&A, 249, 31
Sakamoto, K., Okumura, S. K., Ishizuki, S., & Scoville, N. Z. 1999, ApJS, 124, 403
Sanders, D. B., & Mirabel, I. F. 1996, ARA&A, 34, 749
Sanders, D. B., Mazzarella, J. M., Kim, D.-C., et al. 2003, AJ, 126, 1607
Sato, F., Mizuno, A., Nagahama, T., et al. 1994, ApJ, 435, 279
Scoville, N. Z., & Solomon, P. M. 1974, ApJ, 187, L67
Scoville, N., & Young, J.S. 1983, ApJ, 265, 148
Scoville, N., Yun, M. S., Clemens, D. P., et al. 1987, ApJS, 63, 821
Shetty, R., Glover, S. C., Dullemond, C., et al. 2011, /mnras, 11
Sodroski, T. J., Odegard, N., Dwek, E., et al. 1995, ApJ, 452, 262
Soifer, B. T., Houck, J. R., & Neugebauer, G. 1987, ARA&A, 25, 187
Solomon, P. M., & Sage, L. J. 1988, ApJ, 334, 613
Solomon, P. M., & Vanden Bout, P. A. 2005, ARA&A, 43, 677
Sparke, L. S., & Gallagher, J. S., III 2000, Galaxies in the Universe: An Introduction (1st ed.; Cambridge: University Press)
Taniguchi, Y., Ohyama, Y., & Sanders, D. B. 1999, ApJ, 522, 214
van Dishoeck, E. F., & Black, J. H. 1988, ApJ, 334, 771
Vila-Vilaró, B. 2008, PASJ, 60, 1231
Wilson, T. L., Rohlfs, K., & Hüttemeister, S., 2009, Tools of Radio Astronomy (5th ed.; Berlin:Springer)
Young, J. S., & Scoville, N. Z. 1982, ApJ, 258, 467
Young, J. S., & Sanders, D. B. 1986, ApJ, 302, 680
Young, J. S., & Scoville, N. Z. 1991, ARA&A, 29, 581
Young, J. S., Xie, S., Tacconi, L., et al. 1995, ApJS, 98, 219
Zhang, Z. Y., Gao, Y., & Wang, J. Z. 2010, ScChG, 53, 1357

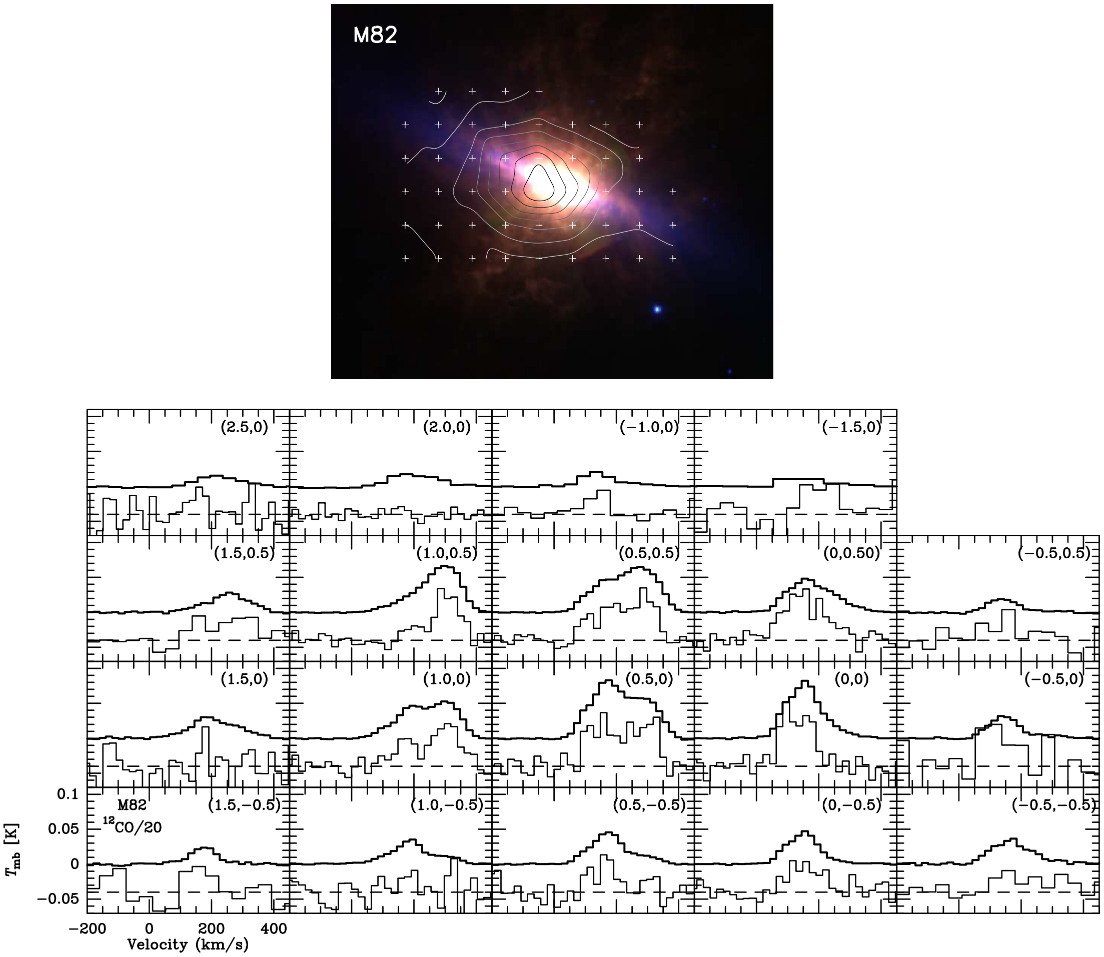

Fig. 1a Spectra of ^{12}CO (*thick lines*) and ^{13}CO (*thin lines*) from the central region of M82 with ^{13}CO tentatively detected. All spectra are on the $T_{\rm mb}$ scale and binned to a velocity resolution of $\sim$20 km s^{-1} (for some weak ^{13}CO emission positions, the spectra are further smoothed to $\sim$40 km s^{-1} for display). ^{12}CO spectra are divided by 20 for comparison purposes. The offset from the center position is indicated in each box. A linear baseline has been subtracted using the line-free portions of each spectrum. M82 was mapped in the $4' \times 2.5'$ central region. The top panel shows the observed positions(crosses) and ^{12}CO contours (contours begin at 10 K km s^{-1} and increase by 40 K km s^{-1} each step) overlaid on infrared image taken from *Spitzer* (8.0 μm (*red*), 5.8 μm (*green*), 3.6 μm (*blue*))

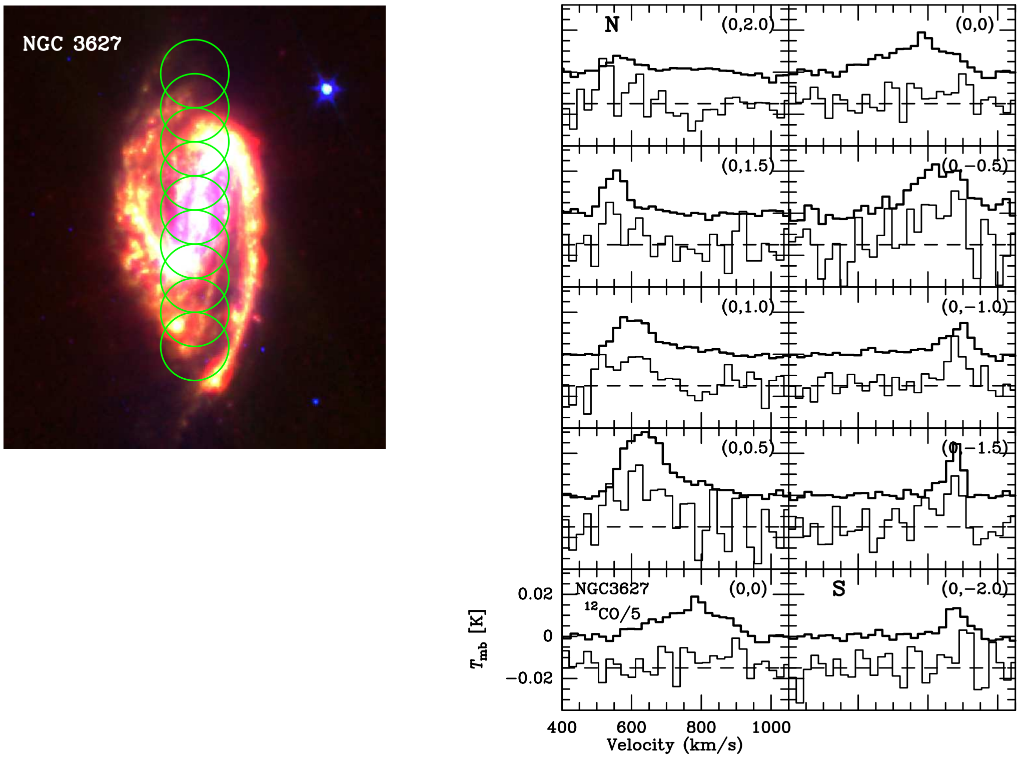

Fig. 1b Same as figure 1a, but for NGC 3627. The spectra were measured along the major (PA=176°) axes of the galactic disk. The left panel shows the half-beam spacing observations overlaid on *Spitzer* infrared image (24.0μm (red),8.0μm ($green$),3.6μm ($blue$)). The size of HPBW ($\sim$60$''$) is represented by circle.

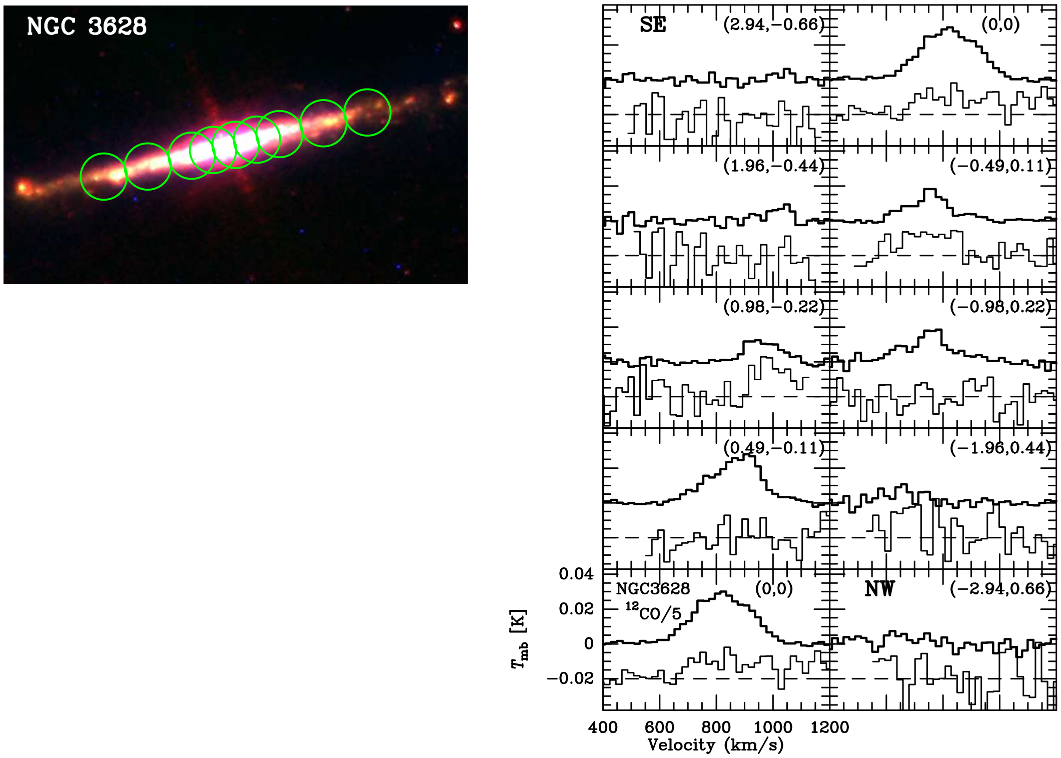

Fig. 1c Same as figure 1b, but for NGC 3628. The spectra were measured along the major (PA=103°) axes of the galactic disk.

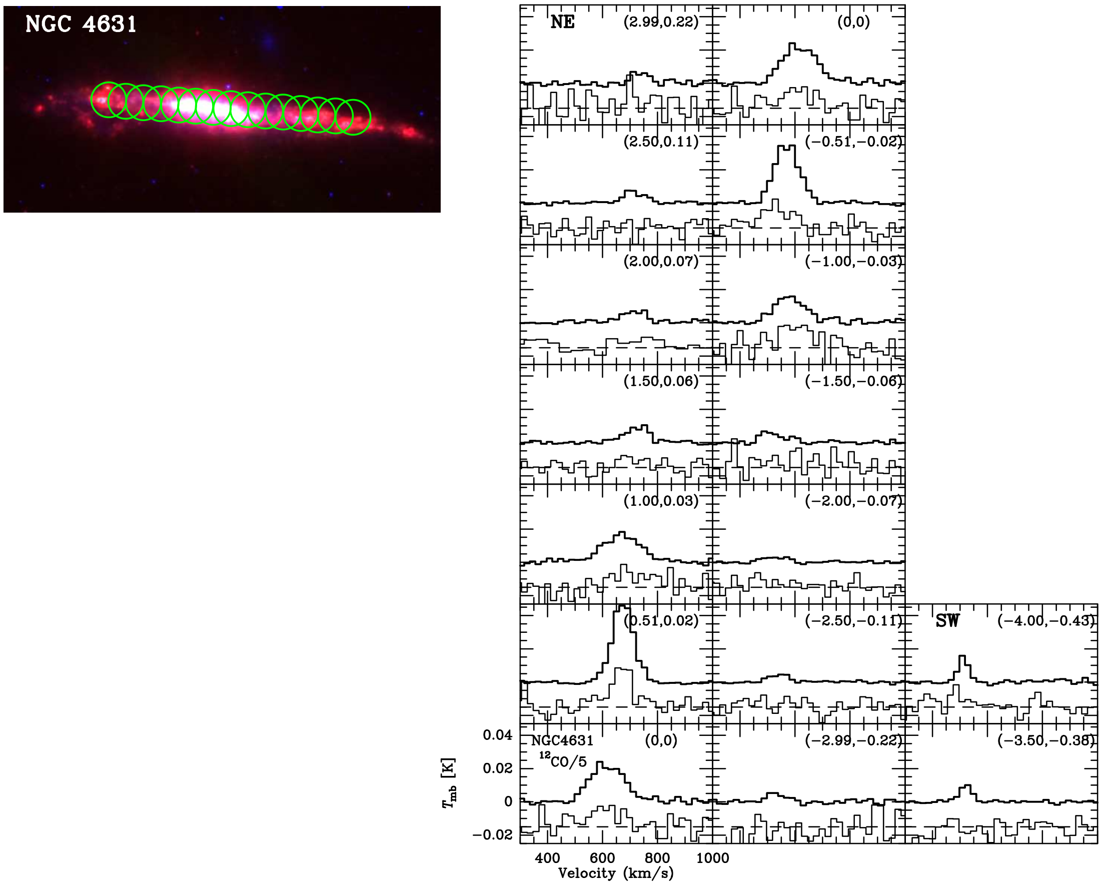

Fig. 1d Same as figure 1b, but for NGC 4631. The spectra were measured along the major (PA=88°) axes of the galactic disk.

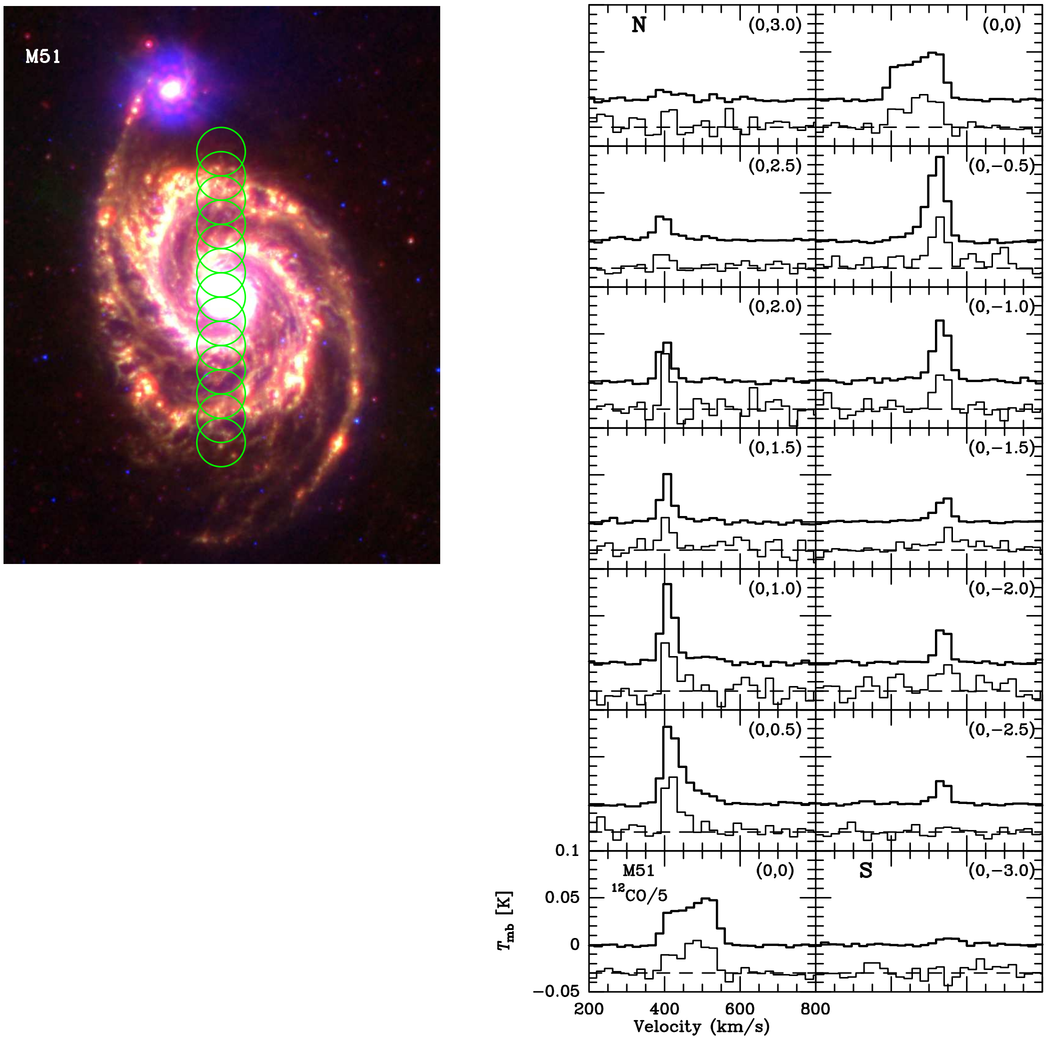

Fig. 1e Same as figure 1b, but for m51. The spectra were measured along the major (PA=0°) axes of the galactic disk.

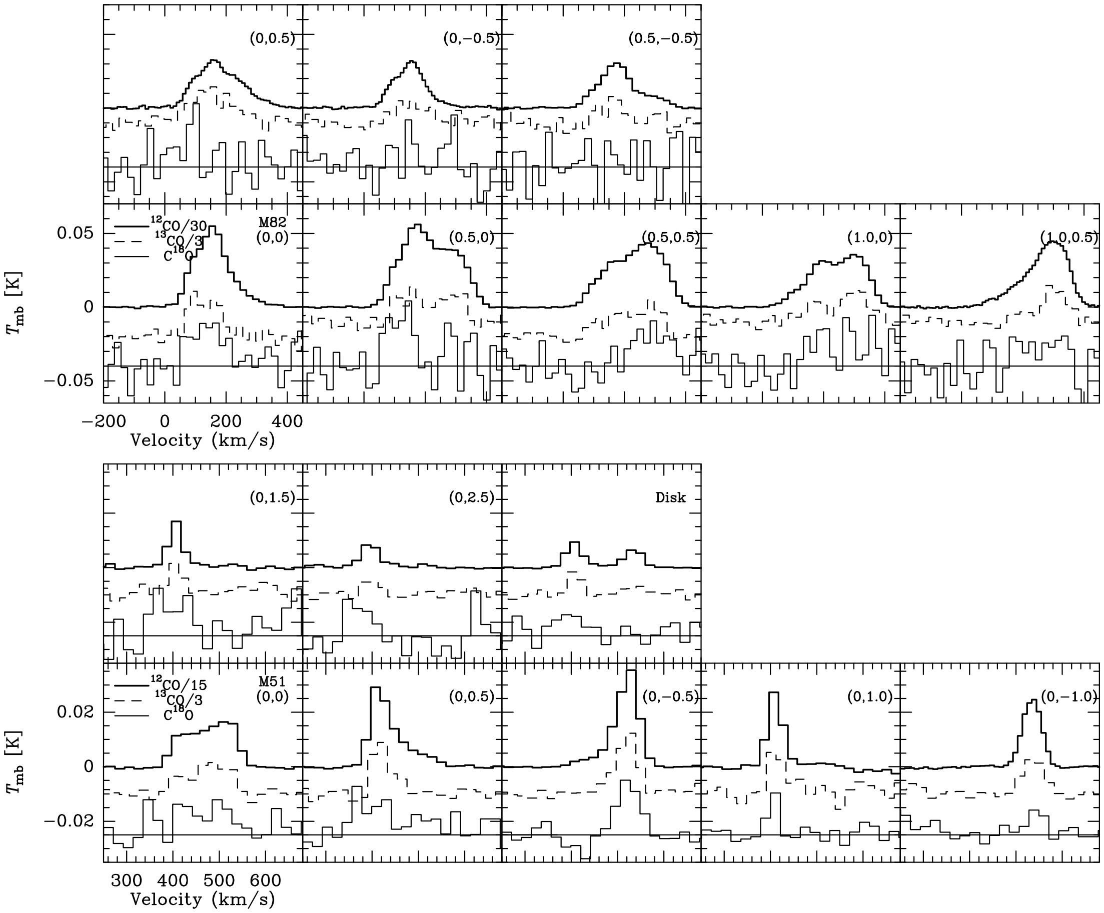

Fig. 2 Spectra of ^{12}CO, ^{13}CO and C^{18}O obtained from the same positions on the galaxy M82 and M51. ^{12}CO spectra are divided by 30 and 15 for display in M82 and M51, while ^{13}CO spectra are divided by 3 for display. M51 disk spectra represent the average emission over the disk region except the center (0,0).

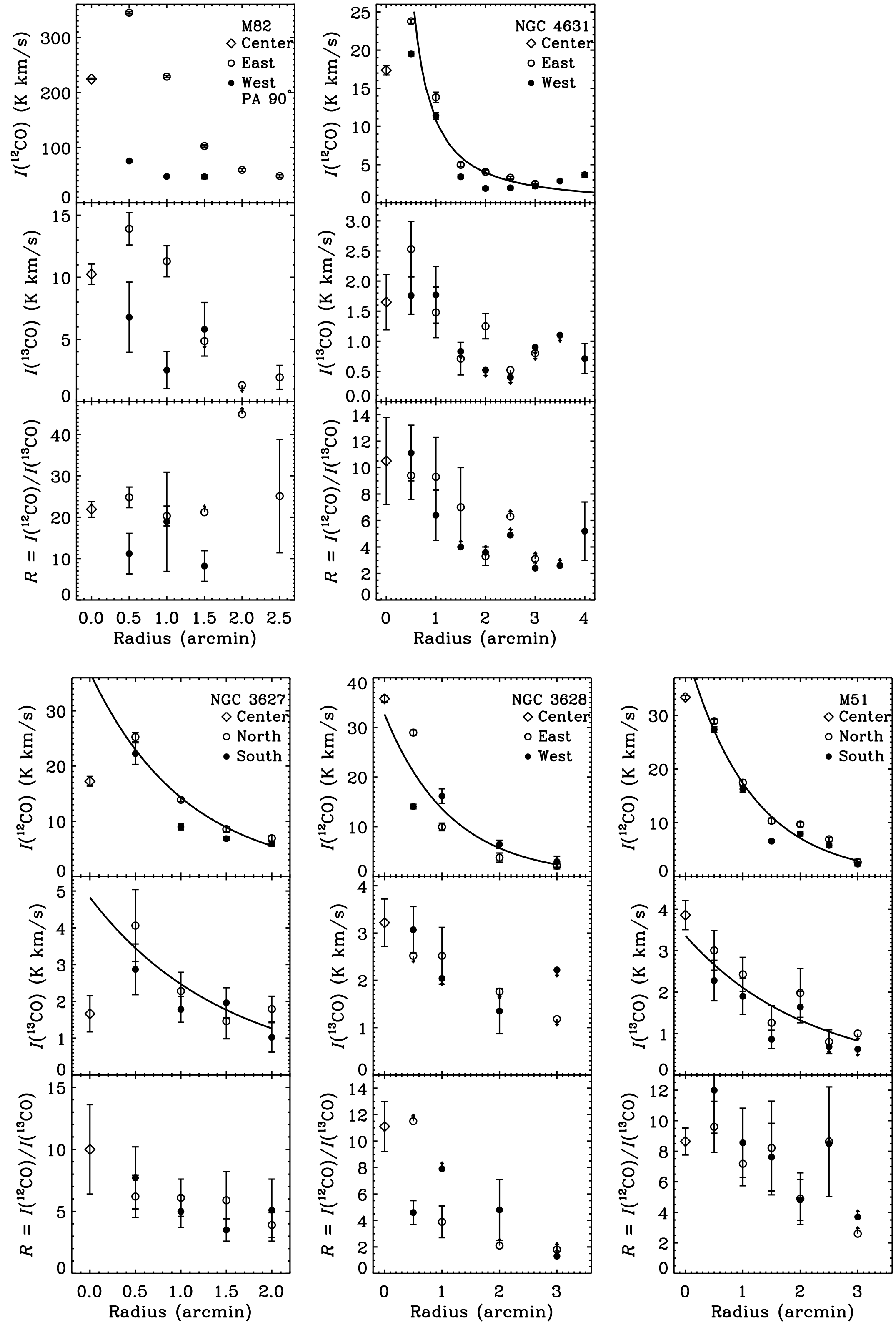

Fig. 3 Radial distributions of ^{12}CO and ^{13}CO integrated intensity and their ratios at each position along the major axes (for M82,the distributions along the axis with position angle of 90 degree are shown). Error bars are 1 σ statistical uncertainty based on the measured rms noise in each spectrum. Upper limits (2σ) are denoted with downward arrow for the non-detection ^{13}CO emission, the corresponding lower limits of line ratio $\mathcal{R}$ are denoted with upward arrow. The solid line in NGC 3627, NGC 3628 and M51 represent the exponential fit to the radial distribution of mean intensity of ^{12}CO and ^{13}CO emission, while in NGC 4631

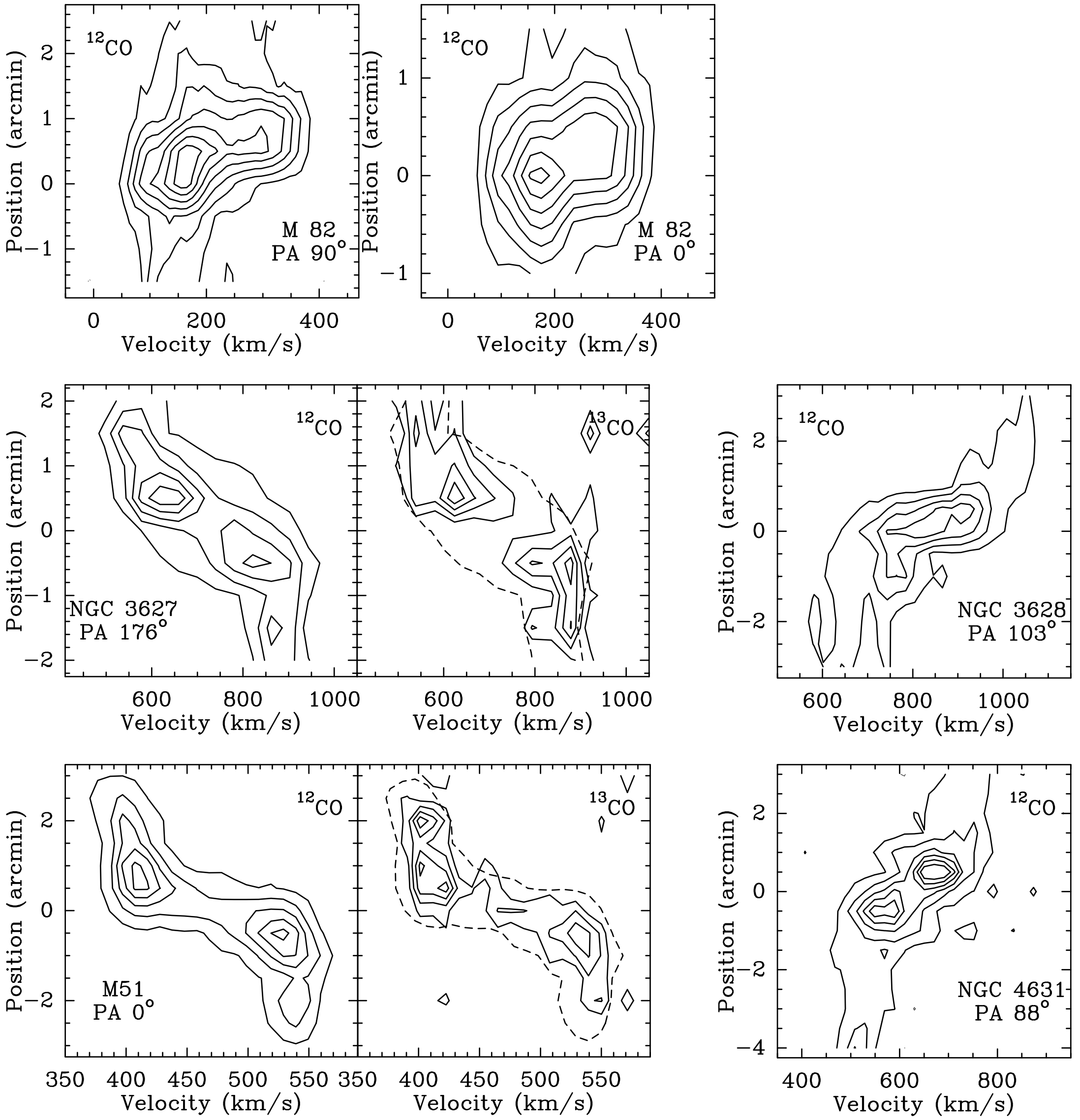

Fig. 4 Position-velocity diagram of ^{12}CO and ^{13}CO (only for NGC 3627 and M51) emission along the major axes of galaxies. For M82, the $P - V$ diagrams with position angle of 0° and 90° are shown. All the spectra were smoothed to have a velocity resolution of $\sim$20 km s^{-1}. The dashed contour on the ^{13}CO panel represents the lowest ^{12}CO contour for comparison.

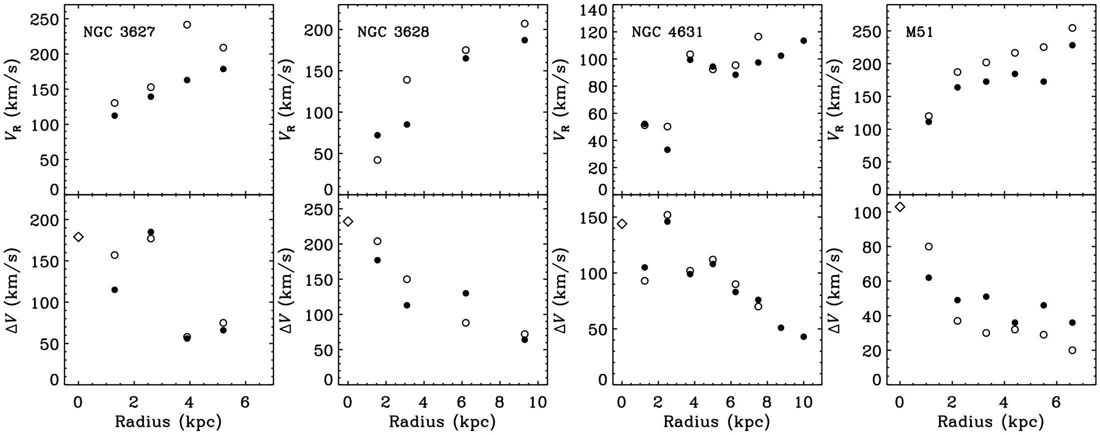

Fig. 5 Rotation velocity derived from ^{12}CO emission line using eq.(8) and line width measured at each position along the major axis. The different symbols represent the same as in Fig.3

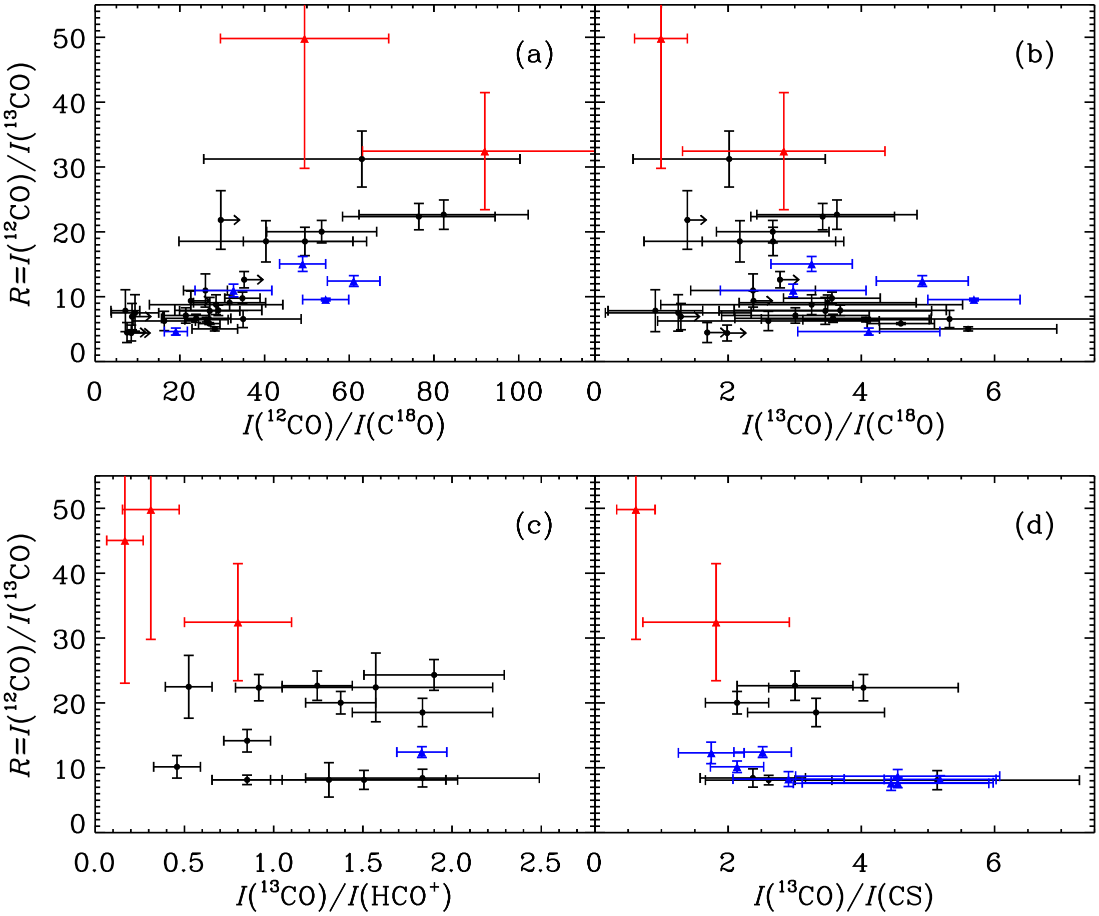

Fig. 6 The relationship for the normal spiral and starburst galaxies between the integrated intensity ratio of ^{12}CO/^{13}CO and a) ^{12}CO/C^{18}O, b) ^{13}CO/C^{18}O, c) ^{13}CO/HCO$^+$, and d) ^{13}CO/CS. The black symbol represents the emission of ^{12}CO, ^{13}CO, and C^{18}O in M82 and M51 (add some new detections in IC 342 and NGC 6949); HCO$^+$ and CS in M82, NGC 3628 and M51. Lower limits (2σ) of ratio are denoted with right pointing arrow for some non-detection C^{18}O emission. The triangle symbol represents the data taken from literatures (see Table 4), the red triangles: NGC 3256, NGC 6240, Arp 220; the blue triangles: NGC 253, NGC 1808, NGC 2146, NGC 4826 and Circinus. Note that all the ratios have been corrected for the different beamsizes.

Table 1 Source List and Galaxy Properties

Source (1)	Alias (2)	R.A. (J2000.0) (3)	Decl. (J2000.0) (4)	V (km s^{-1}) (5)	i (deg) (6)	P.A. (deg) (7)	Type (8)	D_{25} (arcmin) (9)	D (Mpc) (10)	d (kpc) (11)
NGC 2903	UGC 5079	09 32 10.5	+21 30 05.0	556	61	17	SAB(rs)bc, HII	12.6×6.0	7.96	1.9
NGC 3031	M 81	09 55 33.6	+69 03 56.0	−34	58	157	SA(s)ab, LINER/Sy1.8	26.9×14.1	1.00	0.3
NGC 3034	M 82	09 55 49.6	+69 40 41.0	203	80[a]	65[a]	I0, Sbrst/HII	11.2×4.3	2.90	1.3
NGC 3521	UGC 6150	11 05 49.2	−00 02 15.0	805	58	164	SAB(rs)bc, HII/LINER	11.0×5.1	11.47	2.6
NGC 3627	M 66	11 20 15.3	+12 59 32.0	727	63	176	SAB(s)b, LINER/Sy2	9.1×4.2	10.41	2.6
NGC 3628	UGC 6350	11 20 16.2	+13 35 22.0	843	89[a]	103[a]	SAb pec sp, HII/LINER	14.8×3.0	12.07	3.1
NGC 4631	UGC 7865	12 42 07.1	+32 32 33.0	606	85[a]	88[a]	SB(s)d	15.5×2.7	8.67	2.5
NGC 4736	M 94	12 50 52.9	+41 07 15.0	308	35	100	(R)SA(r)ab, Sy2/LINER	11.2×9.1	4.40	1.4
NGC 5055	M 63	13 15 49.5	+42 01 39.0	504	55	105	SA(rs)bc, HII/LINER	12.6×7.2	7.21	2.3
NGC 5194	M 51a	13 29 53.5	+47 11 42.0	463	20[a]	0	SA(s)bc pec, HII/Sy2.5	11.2×6.9	6.62	2.2
NGC 5457	M 101	14 03 09.0	+54 21 24.0	241	27	40	SAB(rs)cd	28.8×26.9	3.45	1.4

[a] From Young et al. (1995).

Notes: Cols.(1) and (2): Galaxy name. Col.(3) and (4): Adopted tracking center. Units of right ascension are hours,minutes,and seconds,and units of declination are degrees,arcminutes,and arcseconds. Col.(5): Heliocentric velocity drawn from the literature and NED. Cols.(6) and (7): Inclination (i) and position angle (P.A.) from Helfer et al.2003, except where noted. Col.(8): Morphological type and nuclear classification from the NED database. Col.(9): Major- and minor- axis diameters from the NED database. Col.(10): Luminosity distance, calculated assuming H_0 = 70 km s^{-1}MPc^{-1}. Col.(11): Linear scale of 60$''$ at distance D, taken from the NED database.

Table 2 Observed and Derived Properties of ^{12}CO and ^{13}CO

			^{12}CO			^{13}CO						
Source	$\Delta\alpha^a$ (arcmin)	$\Delta\delta^a$ (arcmin)	$I_{^{12}\mathrm{CO}} \pm \sigma_I{}^b$ (K km s^{-1})	V^c_{mean} (km s^{-1})	ΔV^c (km s^{-1})	$I_{^{12}\mathrm{CO}} \pm \sigma^b_I$ (K km s^{-1})	V^c_{mean} (km s^{-1})	ΔV^c (km s^{-1})	$\mathcal{R}^d$	$\tau(^{13}\mathrm{CO})^e$	$N(\mathrm{H_2})^f$ (10^{20} cm^{-2})	T^g_k (K)
NGC 2903	0.00	0.00	24.89±0.92	548	155	1.95±0.58	591	151	12.8±4.3	0.08	49.8	55
NGC 3031	0.00	0.00	0.66±0.28	-38	127	< 0.68	...	...	>1.0	...	1.3	...
M82	0.00	0.00	224.61±1.51	159	138	10.25±0.82	126	123	21.9±1.9	0.05	449.2	98
	0.00	0.50	163.0±1.62	180	162	11.80±1.06	153	167	13.8±1.4	0.08	328.8	66
	0.00	-0.50	113.4±1.12	150	115	5.59±0.90	137	150	20.3±3.5	0.05	230.0	110
	0.50	0.00	344.77±2.04	214	184	13.91±1.31	230	194	24.8±2.5	0.04	689.5	111
	0.50	0.50	278.07±1.53	233	183	11.37±0.97	238	180	24.5±2.2	0.04	556.1	110
	0.50	-0.50	134.00±1.50	169	125	5.61±1.10	162	87	23.9±4.9	0.04	269.8	110
	1.00	0.00	228.83±1.66	242	180	11.29±1.25	265	142	20.3±2.4	0.05	457.7	90
	1.00	0.50	218.00±1.69	268	162	6.38±0.83	313	110	34.2±4.7	0.03	435.8	120
	1.50	0.50	92.34±2.04	255	164	6.99±1.01	264	215	13.2±2.2	0.08	184.7	57
	1.50	-0.50	48.95±1.74	173	94	3.64±1.36	158	82	13.4±5.5	0.08	97.9	58
	2.50	0.00	48.64±2.44	219	147	1.94±0.96	158	46	25.1±13.7	0.04	97.3	113
	-0.50	0.00	75.91±1.88	144	112	6.78±2.83	114	100	11.2±5.0	0.09	151.8	48
	-0.50	-0.50	45.75±1.66	140	110	5.75±1.33	226	250	7.9±2.1	0.13	91.5	32
	-1.00	0.00	47.85±1.96	135	104	2.52±1.49	141	44	18.9±12.0	0.05	95.7	84
	-1.50	0.00	47.40±3.86	162	147	5.81±2.16	183	111	8.2±3.7	0.13	94.8	33
NGC 3521	0.00	0.00	22.00±0.37	770	231	2.05±0.66	770	210	10.7±3.7	0.10	44.0	45
NGC 3627	0.00	0.00	17.24±0.87	769	179	1.66±0.49	866	200	10.4±3.6	0.10	34.5	44
	0.00	0.50	25.26±0.83	653	157	4.06±0.98	625	163	6.2±1.7	0.18	50.5	24
	0.00	1.00	13.88±0.38	633	177	2.28±0.51	597	138	6.1±1.5	0.18	27.8	23
	0.00	1.50	8.55±0.52	554	58	1.46±0.48	580	75	5.9±2.3	0.19	17.1	22
	0.00	2.00	6.90±0.50	583	75	1.79±0.35	527	74	3.9±1.0	0.30	13.8	13
	0.00	-0.50	22.25±1.96	827	115	2.87±0.69	829	145	7.7±2.5	0.14	44.5	31
	0.00	-1.00	8.96±0.53	851	185	1.78±0.35	885	91	5.0±1.3	0.22	17.9	18
	0.00	-1.50	6.82±0.31	872	56	1.96±0.41	877	90	3.5±0.9	0.34	13.6	11
	0.00	-2.00	5.90±0.42	886	66	1.02±0.40	902	43	5.1±2.5	0.19	11.8	22
NGC 3628	0.00	0.00	35.80±0.67	823	232	3.22±0.50	839	211	11.1±1.9	0.09	71.6	47
	0.49	-0.11	28.95±0.52	865	204	<2.52	...	...	>11.5	...	57.9	...
	0.98	-0.22	9.95±0.77	962	150	2.52±0.60	986	110	3.9±1.2	0.29	19.9	13
	1.96	-0.44	3.77±0.92	998	88	<1.76	...	...	>2.1	...	7.5	...
	2.94	-0.66	2.13±0.64	1030	72	<1.18	...	...	>1.8	...	4.3	...
	-0.49	0.11	14.06±0.46	751	177	3.07±0.49	745	206	4.6±0.9	0.25	28.1	16
	-0.98	0.22	16.16±1.47	738	113	<2.04	...	...	>7.9	...	32.3	...
	-1.96	0.44	6.45±0.81	658	130	1.35±0.48	675	83	4.8±2.3	0.23	12.9	17
	-2.94	0.66	2.95±1.11	636	64	<2.22	...	...	>1.3	...	5.9	...
NGC 4631	0.00	0.00	17.36±0.62	623	144	1.65±0.46	606	146	10.5±3.3	0.10	34.7	44
	0.51	0.02	23.77±0.24	674	93	2.53±0.46	677	80	9.4±1.8	0.11	47.5	39
	1.00	0.03	13.82±0.67	673	152	1.48±0.42	697	198	9.3±3.0	0.11	27.6	39
	1.50	0.06	4.98±0.26	726	102	0.71±0.27	704	108	7.0±3.0	0.15	9.9	28
	2.00	0.06	4.07±0.25	715	112	1.25±0.21	731	148	3.3±0.7	0.37	8.1	10
	2.50	0.11	3.29±0.19	718	90	<0.52	...	...	>6.3	...	6.6	...
	2.99	0.22	2.48±0.33	739	70	<0.80	...	...	>3.1	...	5.0	...
	-0.51	-0.02	19.50±0.27	571	105	1.76±0.31	528	141	11.1±2.1	0.09	39.0	47
	-1.00	-0.03	11.40±0.44	590	146	1.77±0.47	600	140	6.4±1.9	0.17	22.8	25
	-1.50	-0.06	3.41±0.23	524	99	<0.83	...	...	>4.0	...	6.8	...
	-2.00	-0.07	1.89±0.16	529	108	<0.52	...	...	>3.6	...	3.8	...
	-2.50	-0.11	1.96±0.14	535	83	<0.40	...	...	>4.9	...	3.9	...
	-2.99	-0.22	2.20±0.31	526	76	<0.90	...	...	>2.4	...	4.4	...
	-3.50	-0.38	2.86±0.19	521	51	<1.10	...	...	>2.6	...	5.7	...
	-3.68	-0.30	3.68±0.30	510	43	0.71±0.25	486	34	5.2±2.2	0.21	7.4	19
NGC 4736	0.00	0.00	8.01±0.70	340	153	1.12±0.29	391	114	7.2±2.5	0.15	16.0	28
NGC 5055	0.00	0.00	16.15±1.05	527	214	2.09±0.86	527	275	7.7±3.7	0.14	32.3	31
M51	0.00	0.00	33.35±0.39	475	103	3.86±0.35	472	87	8.6±0.9	0.12	66.7	35
	0.00	0.50	28.90±0.42	434	80	3.01±0.48	425	37	9.6±1.7	0.11	57.8	40
	0.00	1.00	17.45±0.56	410	30	2.43±0.41	408	23	7.2±1.4	0.15	34.9	29
	0.00	1.50	10.35±0.50	406	30	1.26±0.41	409	41	8.2±3.1	0.13	20.7	34
	0.00	2.00	9.70±0.45	401	32	1.98±0.59	406	26	4.9±1.7	0.23	19.4	18
	0.00	2.50	6.90±0.37	398	29	0.80±0.29	396	37	8.6±3.5	0.12	13.8	36
	0.00	3.00	2.62±0.56	388	20	<1.00	...	...	>2.6	...	5.2	...
	0.00	-0.50	27.35±0.53	513	62	2.28±0.49	520	58	12.0±2.8	0.09	54.7	51
	0.00	-1.00	16.25±0.55	534	49	1.90±0.44	536	42	8.5±2.3	0.12	32.5	35
	0.00	-1.50	6.55±0.23	534	51	0.86±0.22	563	53	7.6±2.2	0.14	13.1	31
	0.00	-2.00	7.90±0.37	538	36	1.64±0.38	539	43	4.8±1.3	0.23	15.8	17
	0.00	-2.50	5.77±0.33	534	46	<0.68	...	...	>8.5	...	11.5	...
	0.00	-3.00	2.28±0.35	553	36	<0.62	...	...	>3.7	...	4.6	...
M51 disk^h	…	…	11.85±0.30	462	151	1.73±0.37	411	20	6.8±1.6	0.16	23.7	27
NGC 5457	0.00	0.00	9.82±0.51	255	72	1.97±0.49	277	128	5.0±1.5	0.22	19.6	18

[a] Offset from the nucleus position listed in Table 1, in units of arcminutes.

[b] The measured integrated intensities and associated uncertainties, calculated using the prescription explained in the text. For non-detections, a 2 σ_I upper limit was given.

[c] Velocity and line widths are Gaussian fit values, or else are calculated from the moment for non-Gaussian lines.

[d] The ratio of ^{12}CO to ^{13}CO integrated intensities. The errors are based on the statistical uncertainties of integrated intensities, which can be derived from the error transfer formula $\sigma(\mathcal{R}_{12/13}) = ([\frac{\sigma(I_{12})}{I_{13}}]^2 + [\frac{\sigma(I_{13})\times\mathcal{R}_{12/13}}{I_{13}}]^2)^{1/2}$.

[e] The average optical depth in ^{13}CO emission line, calculated from eq (4).

Table 3 Observed and Derived Properties of $C^{18}O$

Source Source	$\Delta\alpha$ arcmin	$\Delta\delta$ arcmin	$I_{C^{18}O} \pm \sigma_I$ (K km s^{-1})	$V_{\rm mean}$ (km s^{-1})	ΔV (km s^{-1})	$\tau(C^{18}O)^a$	$N(H_2)^b$ (10^{21} cm^{-2})
M82	0.0	0.0	3.81±0.90	140	121	0.017	18.6
	0.0	0.5	<4.2	…	…	…	…
	0.0	-0.5	2.55±1.27	224	176	0.022	14.0
	0.5	0.0	3.80±0.90	145	93	0.011	25.2
	0.5	0.5	3.30±0.76	289	135	0.012	20.5
	0.5	-0.5	<4.1	…	…	…	…
	1.0	0.0	4.19±1.20	284	236	0.018	20.6
	1.0	0.5	3.14±1.84	256	174	0.015	14.8
M51	0.0	0.0	1.04±0.35	466	176	0.032	7.4
	0.0	0.5	0.92±0.49	413	154	0.032	5.7
	0.0	1.0	0.45±0.16	407	23	0.026	4.6
	0.0	1.5	0.99±0.54	393	79	0.10	2.4
	0.0	2.0	<1.17	…	…	…	…
	0.0	2.5	0.88±0.37	369	58	0.14	1.6
	0.0	-0.5	0.95±0.17	519	37	0.035	4.3
	0.0	-1.0	0.55±0.13	544	35	0.034	3.6
	0.0	-1.5	<0.68	…	…	…	…
	0.0	-2.0	<0.84	…	…	…	…

[a] The average optical depth in $C^{18}O$ emission line is calculated from the similar equation as eq.(4).

[b] H_2 column density derived from $C^{18}O$, calculated from eq.(6).

Table 4 Line Intensity Ratios

Source	$\Delta\alpha$ arcmin	$\Delta\delta$ arcmin	$I_{^{12}\mathrm{CO}}/I_{\mathrm{C}^{18}\mathrm{O}}$	$I_{^{13}\mathrm{CO}}/I_{\mathrm{C}^{18}\mathrm{O}}$	$I_{^{13}\mathrm{CO}}/I_{\mathrm{HCO}^{+}}$	$I_{^{13}\mathrm{CO}}/I_{\mathrm{CS}}$	References
M82	0.0	0.0	53.5±13.0	2.7±0.9	1.4±0.2	2.1±0.5	This work
	0.0	0.5	>35.3	>2.8	0.9±0.1	...	This work
	0.0	-0.5	40.5±20.6	2.2±1.4	0.5±0.1	...	This work
	0.5	0.0	82.3±19.5	3.7±1.2	1.2±0.2	3.0±0.9	This work
	0.5	0.5	76.5±18.0	3.4±1.1	0.9±0.1	4.0±1.4	This work
	0.5	-0.5	>29.8	>1.4	1.6±0.7	...	This work
	1.0	0.0	49.5±14.5	2.7±1.1	1.8±0.4	3.3±1.0	This work
	1.0	0.5	63.2±37.5	2.0±1.4	1.9±0.4	...	This work
NGC 3628	0.0	0.0	...	...	0.5±0.1	...	This work
NGC 4631	0.0	0.0	>22.8	>2.4	…	…	This work
M51	0.0	0.0	29.1±10.3	3.7±1.6	0.9±0.2	2.6±0.9	This work
	0.0	0.5	28.6±15.8	3.3±2.3	1.8±0.7	2.4±0.8	This work
	0.0	1.0	34.9±13.7	5.3±2.8	1.3±0.7	...	This work
	0.0	1.5	9.4±5.6	1.3±1.1	...	...	This work
	0.0	2.0	>7.6	>1.7	...	...	This work
	0.0	2.5	7.1±3.4	0.9±0.7	…	…	This work
	0.0	-0.5	26.0±5.2	2.4±0.9	1.5±0.5	5.1±2.1	This work
	0.0	-1.0	27.0±7.1	3.5±1.6	...	...	This work
	0.0	-1.5	>8.7	>1.3	…	…	This work
	0.0	-2.0	>8.6	>2.0	…	…	This work
M51 disk	…	…	16.4±7.4	2.6±1.7	…	…	This work
NGC 253	0.0	0.0	61.0±6.2	4.9±0.7	1.8±0.1	2.5±0.4	1,2,3
NGC 891	0.0	0.0	...	...	...	4.5±1.4	3,4
NGC 1068	0.0	0.0	...	...	...	1.7±0.5	3,5
NGC 1808	0.0	0.0	48.9±5.4	3.3±0.6	...	...	6,7
NGC 2146	0.0	0.0	32.7±9.1	3.0±1.1	...	...	6,7
NGC 2903	0.0	0.0	...	...	...	4.5±1.5	3,4
NGC 3256	0.0	0.0	91.6±28.1	2.9±1.5	0.8±0.3	1.8±1.1	8
NGC 4736	0.0	0.0	...	...	...	4.5±1.5	3,4
NGC 4826	0.0	0.0	19.0±2.7	4.1±1.1	...	...	6,7
NGC 5457	0.0	0.0	...	...	...	2.9±0.8	3,4
NGC 6240	0.0	0.0	...	...	0.2±0.1	...	9
Maffei2	0.0	0.0	...	...	...	5.2±0.8	3,4
IC 342	0.0	0.0	35.1±3.0	3.9±0.3	...	2.1±0.4	1,3,4
Circinus	0.0	0.0	54.4±5.4	5.7±0.7	...	...	6,7
Arp 220	0.0	0.0	49.4±19.9	1.0±0.4	0.3±0.1	0.6±0.3	9

Notes: All the ratios of integrated intensity have been corrected for the different beamsizes.

References: (1) Sage et al. (1991); (2) Henkel et al. (1993); (3) Sage et al. (1990); (4) Sage & Isbell (1991); (5) Young & Sanders (1986); (6) Aalto et al. (1991); (7) Aalto et al. (1995); (8) Casoli et al. (1992); (9) Greve et al. (2009).

Appendix A: THE STABILITY OF DLH RADIO TELESCOPE

Figure A.1 is an Allan Variance Plot, which is often the ultimate way to measure stability but requires an enormous amount of observation time. There are three main contributions to be aware of in the Allan plot, including the white noise, the $1/f$-noise and low frequency drift noise. The upper panel of Fig. A.1 shows that how the squared RMS noise of ^{12}CO spectra with velocity resolution of $\sim$0.16 km s^{-1} varied with the integration time on source, while the lower panel shows the relative error deviate from the radiometer equation. The radiometer equation, also the limiting sensitivity of the spectrometer, is given by

$$\frac{\Delta T_{\rm rms}}{T_{\rm sys}} = \frac{K}{\sqrt{\Delta\nu\tau}}\,, \qquad (A1)$$

where $T_{\rm sys}$ is system temperature, τ is the sum of the integration time on the source and on the off position, K is a factor accounting for data taking procedures, and $\Delta T_{\rm rms}$ is rms noise temperature of the spectra for a given frequency resolution $\Delta\nu$.

Figure A.1a and b show the data obtained from the observing semesters of 2008 to 2009 and of 2009 to 2010, respectively. It can be seen in Figure A.1a that the Allan plot begin to deviate from the radiometer equation when integrating about 10 minutes on source, and the relative error increase to 80% when integrating 100 minutes, however, it is shown in Figure A.1b that the relative error increase to only 10% with the same integration time. Therefore, both the stability and the sensitivity of the telescope have been greatly improved after the system maintenance in the summer of 2009. The average noise level in units of T_A^* would be 0.020 K and 0.018 K when integrating 100 and 200 minutes on source respectively, with spectra velocity resolution of $\sim$10 km s^{-1}. Therefore, this plot can be used to estimate observation time according to the sensitivity that we required. But an important thing to note in this Allan Variance Plot is that the data we used are the raw data, that is to say, we didn't do any data processing such as rejecting the spectra with distorted baseline or abnormal rms noise level. Consequently, we could get even better sensitivity if we just co-added the spectra that found to be consistent within normal rms noise level. Based on these analysis, it seems to imply that the telescope still have the capability to detect even weaker emission signal than what have been detected, since the effective integration time of most of our observations have not reach the limit.

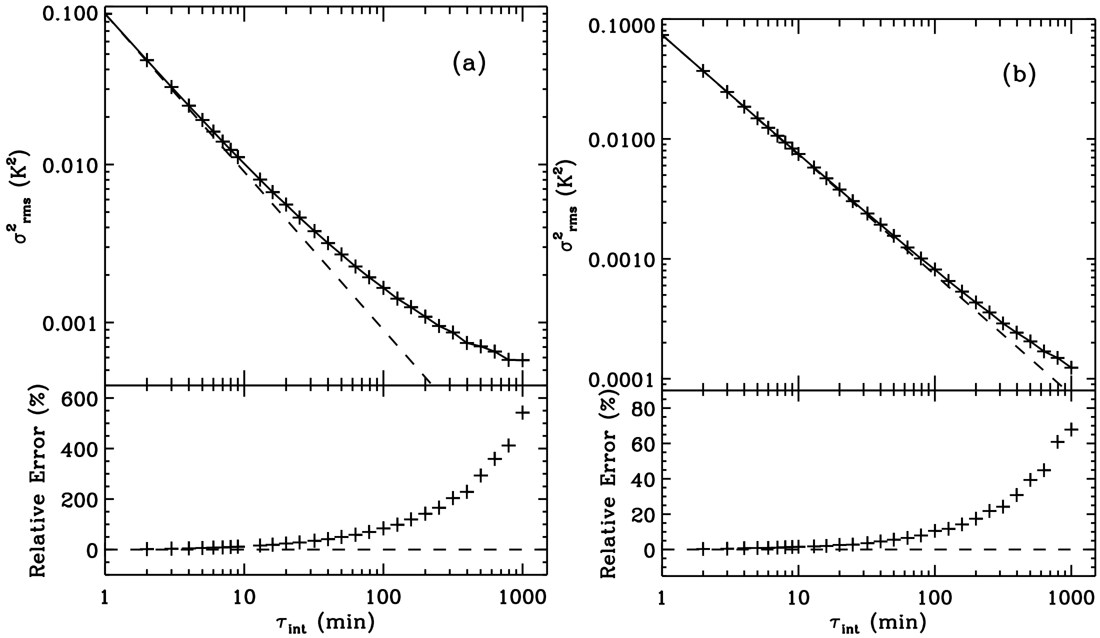

Fig. A.1 The Allan Variance and the relative error from radiometer equation as a function of integration time on source (see Appendix A). On the upper panel of each figure, the dashed line represents what is expected from the radiometer equation with a slope of -1. On the lower panel, each point represent the relative error between the value of measured and expected from radiometer equation. (a)the data taken from the observing semester of 2008 to 2009. (b)the data taken from the observing semester of 2009 to 2010.